

This is a repository copy of *Multiwavelength observations of a new black-widow millisecond pulsar PSR J1544–2555*.

White Rose Research Online URL for this paper: <a href="https://eprints.whiterose.ac.uk/id/eprint/233244/">https://eprints.whiterose.ac.uk/id/eprint/233244/</a>

Version: Published Version

# Article:

Díaz, S.B., Thongmeearkom, T. orcid.org/0000-0002-9285-6724, Phosrisom, A. et al. (20 more authors) (2025) Multiwavelength observations of a new black-widow millisecond pulsar PSR J1544–2555. Monthly Notices of the Royal Astronomical Society, 543 (3). pp. 3019-3034. ISSN: 0035-8711

https://doi.org/10.1093/mnras/staf1544

# Reuse

This article is distributed under the terms of the Creative Commons Attribution (CC BY) licence. This licence allows you to distribute, remix, tweak, and build upon the work, even commercially, as long as you credit the authors for the original work. More information and the full terms of the licence here: https://creativecommons.org/licenses/

## Takedown

If you consider content in White Rose Research Online to be in breach of UK law, please notify us by emailing eprints@whiterose.ac.uk including the URL of the record and the reason for the withdrawal request.



https://doi.org/10.1093/mnras/staf1544

# Multiwavelength observations of a new black-widow millisecond pulsar PSR J1544-2555

S. Belmonte Díaz , 1\*† T. Thongmeearkom, 1.2\*† A. Phosrisom, 1.2\*† R. P. Breton, 1 M. Burgay, 3 C. J. Clark, 4.5 L. Nieder, 4.5 M. G. F. Mayer, 6.7 W. Becker, 6.8 E. D. Barr, 8 S. Buchner, 9 K. K. Das, 10 V. S. Dhillon, 11,12 O. G. Dodge, 1.4.5 E. C. Ferrara, 13,14,15 J.-M. Griessmeier, 16,17 R. Karuppusamy, 8 M. R. Kennedy, 18 M. Kramer, 18 P. V. Padmanabh, 4.5 J. A. Paice, 1,19 A. C. Rodríguez, 10 and B. W. Stappers

Affiliations are listed at the end of the paper

Accepted 2025 September 11. Received 2025 September 8; in original form 2025 April 22

## **ABSTRACT**

We report the discovery of a new black-widow millisecond pulsar, PSR J1544–2555, associated with the Fermi-Large Area Telescope (LAT) source 4FGL J1544.2–2554. Optical, radio, and gamma-ray observations confirmed its nature as a compact spider binary system. Optical photometry from ULTRACAM revealed a ~2.7-h orbital period, guiding MeerKAT observations that detected ~2.4-ms radio pulsations. Subsequent timing campaigns using the Murriyang Parkes Telescope, the Effelsberg 100-m Radio Telescope, and the Nançay Radio Telescope allowed us to obtain a preliminary timing solution, which enabled us to find gamma-ray pulsations. The final timing solution, spanning 16 yr of Fermi-LAT gamma-ray data, also displays orbital period variations typical of spider pulsars. X-ray observations from eROSITA indicate non-thermal emission, but the relatively low count rate prohibits the search for X-ray pulsations. Optical light curve modelling using Icarus suggests the asymmetry is best explained by a spot model, where uneven heating creates localized temperature variations on the companion. While the optical spectra we obtained are compatible with the physical properties we infer for the companion star, they were not of sufficient signal-to-noise to allow for radial velocity measurements, thus limiting constraints on the neutron star's mass. The observed bluer colour near the light curve minimum suggests possible non-thermal emission from intrabinary shocks, supported by the presence of an X-ray source. This discovery exemplifies the proven capability of the Fermi-LAT catalogue in identifying millisecond pulsar candidates and highlights the role of optical surveys in detecting variable sources suitable for radio follow-up.

Key words: binaries: general – pulsars: general – pulsars: individual: PSR J1544 – 2555 – gamma-rays: stars.

## 1 INTRODUCTION

Millisecond pulsars (MSPs) differ from the regular pulsar population due to their fast spin periods and low spin-down rates (Alpar et al. 1982; Backer et al. 1982; Backer, Kulkarni & Taylor 1983). MSPs are thought to be formed in binary systems through the so-called recycling scenario, where accretion from the companion star spinsup the pulsar through mass transfer (Bhattacharya & van den Heuvel 1991). At this stage, the system would be observed as a low-mass X-ray binary (LMXB). The system would return to emit radio pulsations once mass accretion ceases due to the disappearance of the accretion disc (e.g. after the companion no longer overfills its Roche lobe). Therefore, the recycling scenario suggests that there is a link between LMXBs and millisecond radio pulsars, which is evidenced

© The Author(s) 2025.

by the discovery of accreting millisecond X-ray pulsars (Wijnands & van der Klis 1998), followed by the detection of transitional MSPs (tMSPs; Archibald et al. 2009; Papitto et al. 2013; Stappers et al. 2014). tMSPs are binary systems in which a pulsar has been spun-up enough to start emitting radio pulses. However, these systems can transition back to an accretion state, during which material from the companion star obscures or quenches the radio emission.

Spider pulsars are an emerging class of MSP binaries. They contain an MSP and a tidally locked low-mass stellar companion in a compact orbit ( $P_{\rm orb}\lesssim 24$  h; Roberts et al. 2011). The companion mass divides the population into two sub-categories: black-widows contain a lower mass companion ( $\ll 0.1\,{\rm M}_{\odot}$ ) in comparison to redbacks ( $\gtrsim 0.1\,{\rm M}_{\odot}$ ; Roberts 2012). These energetic systems can emit radiation across the entire electromagnetic spectrum. The MSP dominates the gamma-ray and radio emission. Optical emission is dominated by the companion star, which is tidally distorted due to the close orbit and strongly irradiated by the pulsar wind (Djorgovski & Evans 1988). Variability can be observed at a combination of half the orbital period, due to ellipsoidal modulation from tidal distortion, and at the orbital period, due to changes in the visibility of the

<sup>\*</sup> E-mail: sergio.belmontediaz@manchester.ac.uk (SBD); tinn.thongmeearkom@postgrad.manchester.ac.uk (TT); adipol.phosrisom@manchester.ac.uk (AP)

<sup>†</sup> These authors contributed equally to this work.

irradiated companion star when the temperature on the day side is substantially above that of the night side. An intrabinary shock (IBS) is created when the relativistic pulsar wind collides with the companion stellar wind, which dominates the X-ray emission (Arons & Tavani 1993).

The multiwavelength nature of the emission produced by spiders can be used to facilitate their detection. While the presence of an MSP can be confirmed by finding radio or gamma-ray pulsations, discovering new binaries through radio observations is challenging. The tight orbit of these binary systems causes the pulsar to have a relatively large acceleration, hindering the search (Johnston & Kulkarni 1991). Moreover, the material ablated from the companion's surface by the pulsar wind has the potential to block the pulsar's radio emissions, leading to eclipses lasting a substantial portion of the orbit (e.g. Fruchter, Stinebring & Taylor 1988; Lyne et al. 1990; Polzin et al. 2020). An alternative approach is to search for steep-spectrum radio continuum sources. Previous work (Frail et al. 2016) has shown that gamma-ray MSPs often exhibit unusually steep spectral indices  $(\alpha < -2.5)$ , which may make them less affected by tight orbital motions or propagation effects, potentially offering a more reliable way to identify new MSP candidates. Frail et al. (2018) further demonstrated that identifying steep-spectrum sources can help guide deeper pulsation searches for MSPs.

So far, the most efficient way to find spiders has been through their gamma-ray emission. Since the Fermi Gamma-ray Space Telescope started to operate in 2008, the Large Area Telescope (LAT; Atwood et al. 2009) has detected gamma-ray pulsations of more than 300 pulsars (see e.g. Smith et al. 2023; Thongmeearkom et al. 2024). Roughly half are MSPs and half are young pulsars. Unlike young pulsars. MSPs tend to reside at higher Galactic latitudes due to their advanced age, which provides them with more time to migrate away from the Galactic plane. Traditional radio pulsar surveys have primarily focused on the Galactic plane (e.g. Manchester et al. 2001; Keith et al. 2010), leaving high-latitude regions less explored. The wide field of view of Fermi and its ability to scan the entire sky every 3 h make it particularly effective at identifying gamma-ray emission from pulsars over the whole sky. The spectral characteristics of gamma-ray emission from unidentified sources detected by Fermi provide a powerful means of identifying pulsar-like candidates, which can then guide targeted follow-up searches for pulsations with deep radio observations (e.g. Ray et al. 2012; Clark et al. 2023b). In addition, optical and X-ray observations provide further means of uncovering potential counterparts and characterizing these systems (e.g. Lu et al. 2024; Mayer & Becker 2024). The fourth release of the Fermi-LAT source catalogue (4FGL-DR4; Abdollahi et al. 2020; Ballet et al. 2023) contains more than 7000 sources, of which around 2600 remain unidentified. While many of these are likely active galactic nuclei, they still offer a promising pool for potential pulsar discoveries.

One important property of spider pulsars is their tendency to host heavier pulsars. Based on a sample of 15 objects, Strader et al. (2019) reported a median mass of  $1.78 \pm 0.09 \, M_\odot$  in redback systems, which is significantly larger than the canonical neutron star mass of  $1.4 \, M_\odot$ . High pulsar masses help constrain the equation of state of multiple theoretical models, providing useful insights into the properties of cold, ultradense matter (see Özel & Freire 2016). Some systems have been found to possibly host a neutron star of mass  $\gtrsim 2.1 \, M_\odot$ , such as the black-widows PSR J0952-0607 (2.35  $\pm$  0.17  $M_\odot$ ; Romani et al. 2022), PSR J1653-0158 (2.17  $\pm$ 

 $0.2\,M_\odot$ ; Nieder et al. 2020b), and PSR J1810+1744 (2.13  $\pm$  0.04  $M_\odot$ ; Romani et al. 2021), and the extremely irradiated redback PSR J2215+5135 (2.27  $\pm$  0.16  $M_\odot$ ; Linares, Shahbaz & Casares 2018). The current limitation on these mass measurements is that they rely on the light curve and spectral modelling to infer the orbital inclination and companion's semimajor axis, where systematic uncertainties are still difficult to ascertain especially when light curves present asymmetries. Clark et al. (2023a) recently used gamma-ray eclipses to independently constrain the inclination of spider binaries, which resulted in a reduction in mass for the pulsar PSR B1957+20 from  $2.40 \pm 0.12\,M_\odot$  (van Kerkwijk, Breton & Kulkarni 2011) to  $1.81 \pm 0.07\,M_\odot$  (see also the case for PSR J1311-3430 in Romani, Filippenko & Cenko 2015).

In this paper, we present the discovery of a new black-widow MSP associated with the Fermi-LAT source 4FGL J1544.2-2554. A colocated source showing optical variability of  $\sim$ 2.7 h was found from multiband light curves obtained from ULTRACAM observations. The light curve shows properties that are in agreement with blackwidow systems. The nature of the source was confirmed with the discovery of  $\sim$ 2.4 ms radio pulsations from MeerKAT observations. Independently from this work, Karpova et al. (2024) proposed that 4FGL J1544.2-2554 is a spider candidate with period 2.7 h based on a single-peak optical light curve from the 2.1-m Observatorio Astronomico Nacional San Pedro Martir (OAN-SPM) telescope. In addition, this source was considered a pulsar-like candidate from Xray emission detected with the eROSITA telescope (Mayer & Becker 2024). Some previously identified black-widow systems were first discovered through optical observations and subsequently confirmed via gamma-ray pulsation searches (see Pletsch et al. 2012; Nieder et al. 2020b). However, to our knowledge, this is the first black-widow system to be confirmed through radio follow-up observations after being initially identified as an optical candidate. Notably, redback systems PSR J2339-0533 (Romani & Shaw 2011; Kong et al. 2012; Ray et al. 2020), PSR J0212+5320 (Li et al. 2016; Linares et al. 2017; Perez et al. 2023), and the three pulsars discovered in Thongmeearkom et al. (2024) followed a similar discovery path. Searching for black-widows through optical observations is challenging because they are typically faint sources, requiring the use of highly sensitive telescopes.

# 2 OPTICAL DISCOVERY

The *Fermi*-LAT unidentified source 4FGL J1544.2–2554 was deemed a pulsar candidate based on its gamma-ray spectral properties. Pulsars tend to show low long-term gamma-ray variability and a curved spectrum that deviates from a single power law at high photon energies (Abdo et al. 2010). These features distinguish them from the other main class of gamma-ray sources: active galactic nuclei, which show variability over time and have a flatter spectrum (Parkinson et al. 2016).

The field was observed as part of a survey we conducted to search for periodic optical sources in 35 Fermi-LAT unidentified sources (Phosrisom et al. in preparation) using ULTRACAM (Dhillon et al. 2007), a high-speed imaging photometer mounted at the 3.5-m New Technology Telescope at the European Southern Observatory in Chile (Tarenghi 1986). The observing area was centred at the middle of the Fermi-LAT localization ellipse containing the 95 per cent confidence level of the source's location. The field was observed at Super Sloan Digital Sky Survey bands  $u_s, g_s, r_s$  simultaneously, with exposure times of approximately 20 s, and a dead time of only 24 ms between each exposure. Observations were conducted for a total of 9 h between April and June 2022, with an additional 2 h

<sup>&</sup>lt;sup>1</sup>https://fermi.gsfc.nasa.gov/ssc/data/access/lat/14yr\_catalog/

**Table 1.** Time and orbital phase coverage of the ULTRACAM observations of 4FGL J1544.2–2554. The orbital phase coverage was obtained using the timing solution reported in Table 3.

Start time (UTC)	Observation length (min)	Orbital phase coverage
03-04-2022 06:00:00	60.0	0.38-0.74
04-04-2022 05:04:00	56.0	0.84 - 1.19
05-04-2022 05:02:00	58.0	0.64 - 0.99
06-04-2022 05:09:49	50.5	0.50 - 0.81
07-04-2022 05:02:42	58.5	0.27 - 0.62
29-04-2022 03:59:54	58.3	0.73 - 1.08
30-06-2022 03:02:28	179.3	0.65 - 1.75
11-02-2024 06:17:15	149.2	0.12 - 1.03

and 30 min of observation in February 2024, as shown in Table 1. Data were recorded under photometric conditions, with atmospheric seeing fluctuating from 1 to 1.5 arcsec. Observations were taken at different sidereal times and spread over several weeks to reduce potential aliasing effects when searching for periodic signals. The final set of observations, conducted long after the initial epochs, was used to constrain the orbital period ( $P_{\rm orb}$ ) of potential candidates.

The HiPERCAM (Dhillon et al. 2021) pipeline<sup>2</sup> was used to reduce the data. A Lomb–Scargle periodogram (Lomb 1976; Scargle 1982) was used to search for periodic variability ranging from 1 to 48 h. This is the period range at which spiders are expected to be detected in optical frequencies. In addition to analysing the best two periods of the search, a fold was done at double and half their values to ensure the fundamental period was found. This is motivated by spider pulsar systems showing both single and double-peak light curves. Each source was individually inspected to assess its nature.

A source was found to show a single-peak light curve with a period of  $\sim$ 2.7 h (Fig. 1). The values of the orbital period and large optical variability ( $\gtrsim$  3 mag) presenting a single peak per cycle are in agreement with the candidate being a black-widow pulsar binary (e.g. Mata Sánchez et al. 2023). A Gaia counterpart was also found and provides an accurate position, beneficial for eventual radio timing. A finder chart with the localization of the source and a Lomb-Scargle periodogram are shown in Fig. 2. The long baseline of 1.85 yr between observations helped reduce aliasing in the periodogram and provided an accurate orbital period  $P_{\text{orb}} =$ 0.11349520(4) d (3 ms uncertainty). Modelling the light curve with a simple two-term sinusoid,  $A_0 + A_1 \sin(2\pi(t - T_{asc})/P_{orb} + \pi) +$  $A_2 \cos (4\pi (t - T_{\rm asc})/P_{\rm orb})$ , representing the mean flux, the irradiation and the ellipsoidal variability enables ones to determine the epoch of ascending node of the unseen compact object<sup>3</sup>  $T_{asc} =$ MJD 59672.32042(7) (6 s uncertainty). This statistical uncertainty reflects the fit of a simple symmetric heating model to the light curve. However, deviations from a perfectly symmetric heating distribution could introduce bias in  $T_{\rm asc}$  (see Section 6 for evidence of a slight asymmetry in the light curve).

4FGL J1544.2–2554 was also observed with the Keck I telescope using the Low-Resolution Imaging Spectrometer (LRIS; Oke et al. 1995) on 2024 February 8 and 2024 February 15 (UT). On the first night, we used the 600/4000 grism on the blue side with  $2\times2$  binning (spatial, spectral), and the 400/8500 grating on the red side with  $2\times1$  binning. On the second night, we used the 400/3400 grism on the blue side with  $2\times2$  binning (spatial, spectral), and the 400/8500 grating

on the red side with  $2 \times 1$  binning. On both occasions, we used a 1.0 arcsec slit, and the seeing each night was approximately 0.7–1 arcsec, leading to minimal slit losses. All Keck I/LRIS data were reduced with lpipe, an IDL-based pipeline optimized for LRIS long slit spectroscopy and imaging (Perley 2019). Data were flat fielded sky-subtracted, and heliocentric corrected using standard techniques. Internal arc lamps were used for the wavelength calibration and a standard star for overall flux calibration.

## 3 DISCOVERY OF RADIO PULSATIONS

Given the evidence provided by the optical light curve from the ULTRACAM observations and by the gamma-ray spectrum from *Fermi*-LAT, there is a high likelihood that 4FGL J1544.2–2554 contains a spider pulsar binary. We therefore decided to observe this field with the MeerKAT telescope and search for radio pulsations, as a detection would confirm the presence of an MSP and elucidate the true nature of the gamma-ray point source.

MeerKAT is an interferometer array telescope located in the Karoo, in the Northern Cape of South Africa. Locating the telescope in a remote area reduces radio frequency interference (RFI) to low levels, which makes the MeerKAT telescope a great tool for radio astronomy. It contains 64 steerable radio antennas with a diameter of 13.5 m. All antennas are equipped with *S* band (1750–3500 MHz), *L* band (856–1712 MHz), and Ultra High Frequency (UHF) (544–1088 MHz) receivers, offering a wide range of frequency coverage (Jonas & MeerKAT Team 2016). MeerKAT provides an increase in sensitivity concerning previous radio telescopes in the Southern hemisphere, allowing us to find fainter pulsars.

## 3.1 Observation configuration

We observed the candidate at UHF since pulsars often show steep radio spectra, increasing their detectability at low frequencies (Jankowski et al. 2017). The optical ephemeris provided an approximate orbital period and reference orbital phase, which were used to schedule the observation around the inferior conjunction of the pulsar, where radio eclipses are less likely to occur as the companion is located behind. Following the survey configuration in Thongmeearkom et al. (2024), we scheduled a 1-h radio observation that covers  $\sim$ 35 per cent of the orbit. The extent of orbital coverage enables the system to be observed predominantly during non-eclipsing orbital phases, even if the orbital ephemeris deviates slightly from the actual parameters. At the time of the observation, 60 MeerKAT dishes were available. Since the optical counterpart offers a highly accurate localization, a single tied-array beam was used. The data were recorded at a sampling time of 60 µs and 4096 frequency channels on the 7th of June of 2023 (MJD 60,102).

# 3.2 Pulsation searches

We performed the search using PEASOUP<sup>4</sup> (Barr 2020), a code accelerated using graphics processing units (GPUs) that performs a time-domain resampling acceleration search. The software implements a dedispersion step, dereddening, and an fast Fourier transform (FFT)-based acceleration search through time-domain resampling with incoherent harmonic summing (described in detail in Morello et al. 2018).

<sup>&</sup>lt;sup>2</sup>https://cygnus.astro.warwick.ac.uk/phsaap/hipercam/docs/html/

<sup>&</sup>lt;sup>3</sup>This is to follow orbital phase convention used for pulsar timing.

<sup>&</sup>lt;sup>4</sup>https://github.com/ewanbarr/peasoup

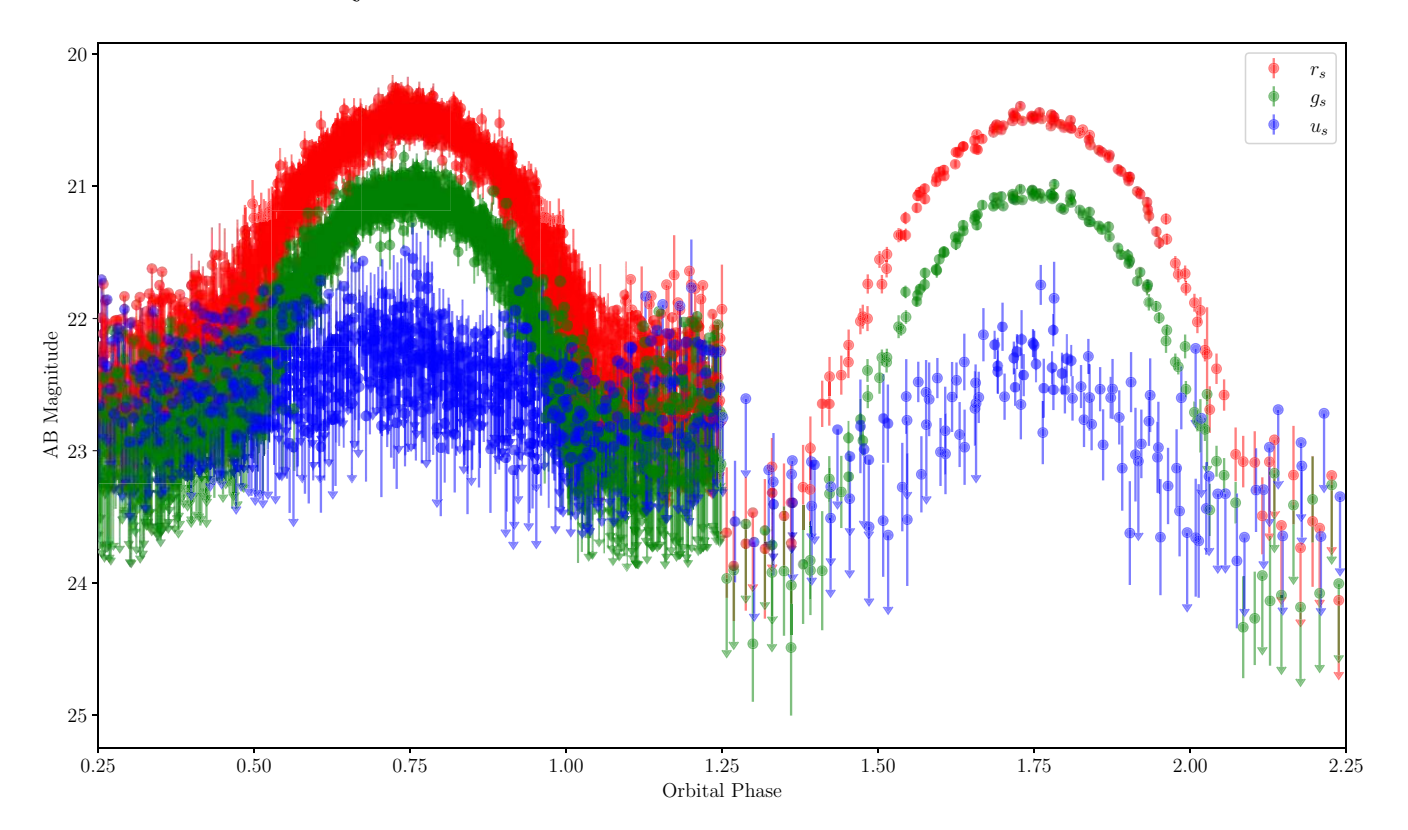


**Figure 1.** ULTRACAM optical light curve of the periodic source in the  $r_s$ ,  $g_s$ , and  $u_s$  bands folded at the best orbital period found from the Lomb–Scargle periodogram (0.113495 d). In the first cycle (left), all available data points are plotted and in the second cycle (right) data points are averaged to ease the visualization of the light curve's trend. Orbital phases are defined such as 0.25 corresponds to the pulsar's superior conjunction.

We search for radio pulsations over a dispersion measure (DM) range of 0–180 pc cm<sup>-3</sup>, with a DM step of 0.1 pc cm<sup>-3</sup>; and over accelerations up to 50 m s<sup>-2</sup>. The DM range was chosen by considering twice the maximum amount of dispersion predicted from the electron density models YMW16 (Yao, Manchester & Wang 2017) and NE2001 (Cordes & Lazio 2002) to ensure the real DM is not missed. The acceleration limit was chosen considering the maximum acceleration a spider pulsar can experience given an approximate orbital period, pulsar mass, and companion mass typical of these systems. We coherently searched in the full-hour observation and in 30- and 15-min segments. The search in the shorter segments was motivated by the fact that shorter observing lengths enhance the detection of pulsars in tight orbits, where optimal observation times for MSPs with orbits of less than a day range from 5 to 20 per cent of the orbital period (Johnston & Kulkarni 1991).

We initially found a candidate with a period of  $\sim$ 2.4 ms in one of the 15-min segments. Further analysis of the full hour revealed it in other segments. The short period and the large acceleration ( $\sim$ 15.8 m s<sup>-2</sup>) confirms the binary nature of this new MSP.

# 3.3 Radio timing

We initiated a timing campaign for PSR J1544–2555 using the Murriyang Parkes telescope,<sup>5</sup> the Effelsberg 100-m radio telescope,<sup>6</sup> and the Nançay Radio Telescope (NRT; Guillemot et al. 2023). Timing of a pulsar binary system involves fitting the pulse times

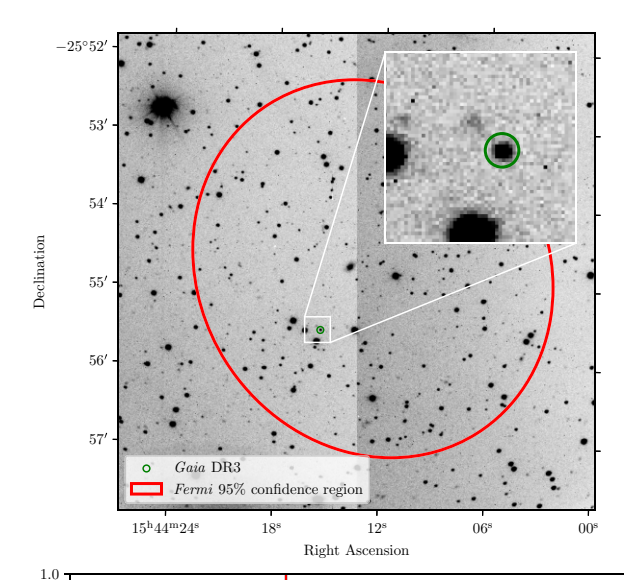
of arrival (TOAs) with a model parametrized by the spin period (P), DM, orbital period ( $P_{\rm orb}$ ), epoch of ascending node ( $T_{\rm asc}$ ), projected semimajor axis (x) and the source's sky position.

The discovery time-versus-spin-phase plot showed a curved pulsar signal, indicating that the folding parameters found by the acceleration search software were not optimal. To refine these parameters, we measured the pulsar's spin period across the 1-h MeerKAT observation using PREPFOLD from PRESTO<sup>7</sup> (Ransom 2011) on 5-min segments. The short segment duration allowed accurate determination of the spin period at different orbital phases. The barycentric spin periods obtained were fitted for a circular orbit using fit\_circular\_orbit.py from PRESTO, yielding improved values for x,  $P_{\text{orb}}$ , and  $T_{\text{asc}}$ . However, we found that the estimate of  $P_{\text{orb}}$  derived from the optical periodogram (see Section 2) was more accurate than the estimate from fit\_circular\_orbit.py, due to the limited initial radio detections and the longer baseline of optical observations. Therefore, the  $P_{\rm orb}$  from the optical periodogram and the x value from fit\_circular\_orbit.py were used as starting parameters for timing follow-up observations with tempo2 (Hobbs, Edwards & Manchester 2006). The sky position was fixed to the value from Gaia, the DM to the value maximizing the signal-to-noise ratio (S/N) in the full MeerKAT observation, and  $P_{orb}$  to the optical periodogram value. To account for time delays between observations with different telescopes, a 'JUMP' parameter was included in the timing model, allowing for spin-phase adjustments between TOAs from different instruments. Table 2 shows the number of observations, observing time, and number of TOAs for each telescope. The number of TOAs depended on the brightness of the observation. Note

<sup>&</sup>lt;sup>5</sup>https://www.csiro.au/en/about/facilities-collections/ATNF/Parkes-radio-telescope-Murriyang

<sup>&</sup>lt;sup>6</sup>https://eff100mwiki.mpifr-bonn.mpg.de/doku.php

<sup>&</sup>lt;sup>7</sup>https://github.com/scottransom/presto



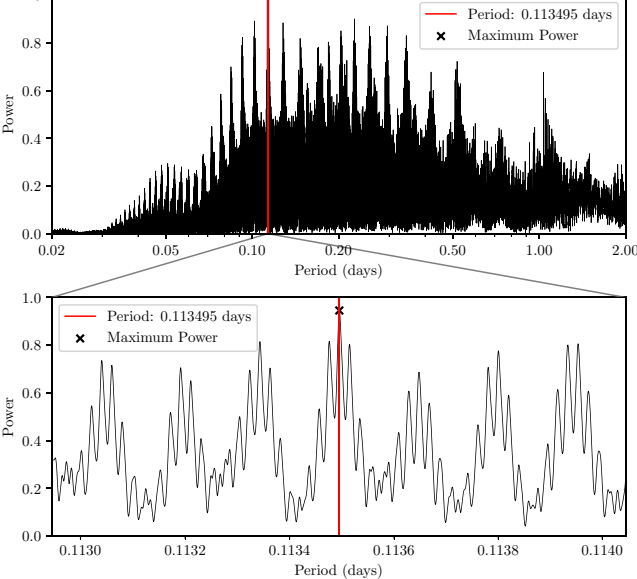


**Figure 2.** Top: Finding chart showing the location of the periodic variable source in the ULTRACAM observing field. The *Fermi*-LAT localization ellipse containing the 95 per cent confidence level of the location of the source is shown as a solid ellipse. The location of the *Gaia* counterpart is indicated by a solid circle. Middle: Full Lomb–Scargle periodogram computed using the data recorded from the optical observations, shown over the period range 0.02–2 d. The vertical line shows the best recovered period. Bottom: Zoomedin view of the Lomb–Scargle periodogram around the best-recovered period. The vertical line shows the best recovered period, and the black cross shows the maximum power at the best orbital period.

**Table 2.** Timing observation table containing the number of observations (N. obs), the total duration of the observations (tobs), and the number of TOAs (N. TOAs) used to obtain the radio timing solution. The information is provided for the different instruments used to observe the source: MeerKAT (MKT), Parkes (PKS), Nançay (NRT), and Effelsberg (EFF). Observations with weak detections, non-detections, and the last Parkes detection (see Fig. 3) are not included in the total counts since they were not used to obtain the timing solution

Telescope	N. obs	tobs (h)	N. TOAs
MKT	1	1	60
PKS	3	3	26
NRT	2	2	14
EFF	1	1	2

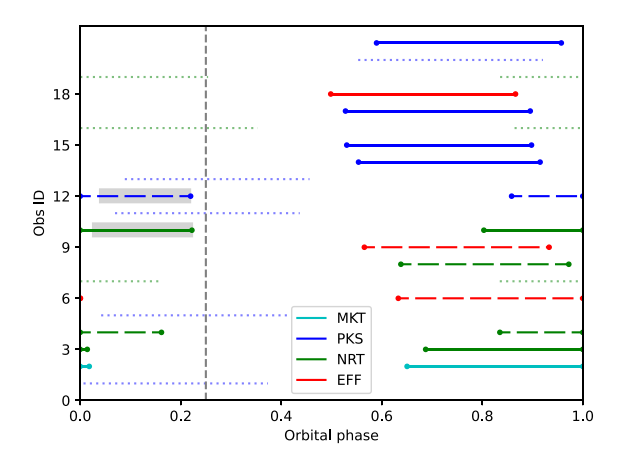


**Figure 3.** Orbital phase coverage of radio observations obtained with different telescopes: MeerKAT (MKT) in cyan, Parkes (PKS) in blue, Nançay (NRT) in green, and Effelsberg (EFF) in red. Phase 0 corresponds to the pulsar at the ascending node, and phase 0.25 corresponds to the pulsar's superior conjunction. Strong detections are displayed by brighter solid lines, while weak detections and non-detections are displayed with a dimmer dashed and dotted line, respectively. Only strong detections were used for pulsar timing (Table 2). The grey-shaded region indicates when a clear eclipse was detected in the observation.

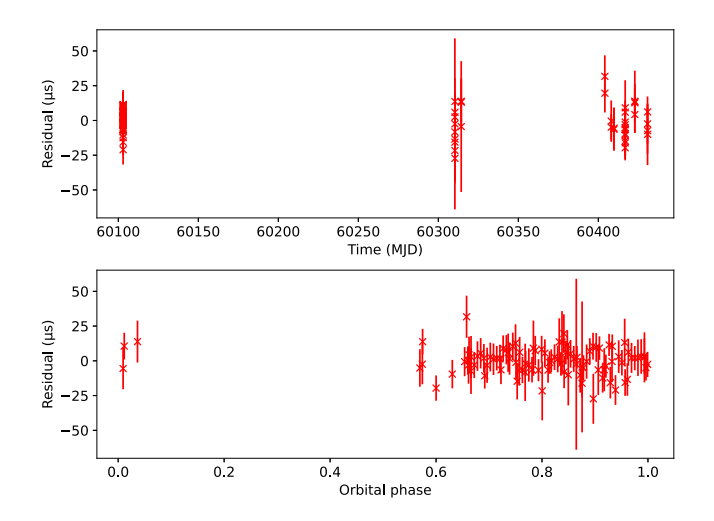


**Figure 4.** Radio residuals for PSR J1544-2555 using the best ephemeris obtained in the joint radio and gamma-ray timing analysis (Table 3), shown versus time (top panel) and orbital phase (bottom panel).

that we did not include TOAs from observations in which the pulsar was very weak (with a PRESTO S/N below 6) as they tend to produce poor results. Fig. 3 illustrates the orbital phase coverage of the observations, with non-detections and weak detections highlighted by different colour markers and line styles. We managed to connect the MeerKAT discovery observation from June 2023 to the latest Effelsberg observation in May 2024 (see the radio residuals in Fig. 4). The timing solution for PSR J1544–2555 is shown in Table 3.

Spider systems are known to exhibit long-term orbital period variations (e.g. Arzoumanian, Fruchter & Taylor 1994; Voisin, Breton & Summers 2020a; Thongmeearkom et al. 2024) (see also Section 4). High orbital frequency derivatives can reduce the S/N of the folded pulse due to small changes in the orbital period. This effect can be mitigated by shifting the reference spin phase iteratively until the signal is recovered. To investigate whether the non-detections

# 3024 S. Belmonte Díaz et al.

**Table 3.** Timing solution for the new black-widow PSR J1544–2555 using joint radio and gamma-ray timing with *Gaia* positional parameters as priors. The derived parameters were obtained following the standard formulae (e.g. Smith et al. 2023), assuming the YMW16 distance. The derived pulsar energetics are corrected for the Shklovskii effect (Shklovskii 1970) and Galactic acceleration (e.g. Damour & Taylor 1991).

Parameter	Value			
Gaia DR3 astrometry				
RA, α (J2000)	15 <sup>h</sup> 44 <sup>m</sup> 15 <sup>s</sup> .4547(1)			
Dec., δ (J2000)	$-25^{\circ}55'32''.688(2)$			
Epoch of position measurement (MJD)	57388.0			
Timing parameters				
Solar-system ephemeris	DE421			
Time-scale	TDB			
Data span (MJD)	54683 - 60560			
Epoch of spin period measurement (MJD)	60103.0			
Proper motion in $\alpha$ , $\mu_{\alpha} \cos \delta$ (mas yr <sup>-1</sup> )	$-5.27 \pm 0.84$			
Proper motion in $\delta$ , $\mu_{\delta}$ (mas yr <sup>-1</sup> )	$-18.1 \pm 2.8$			
Spin frequency, $f$ (Hz)	418.39828661948(4)			
Spin-down rate, $\dot{f}$ (Hz s <sup>-1</sup> )	$-2.0383(2) \times 10^{-15}$			
Dispersion measure, DM (pc cm <sup>-3</sup> )	$25.817 \pm 0.060$			
Orbital period, $P_{\text{orb}}$ (d)	0.113495141(9)			
Projected semimajor axis, x (lt-s)	0.128832(5)			
Epoch of ascending node, $T_{\rm asc}$ (MJD)	56667.87739(9)			
Hyperparameters of orbital-phase-covariance function				
Amplitude of OPV, $h$ (s)	$2^{+2}_{-1}$			
Length scale of OPV, $\ell$ (d)	$1920_{-670}^{-14510}$			
Smoothness parameter, v	> 2.6			
Derived parameters				
Distance, d (kpc), NE2001	1.06			
Distance, d (kpc), YMW16	1.02			
Spin period, $P$ (ms)	2.3900671488879(3)			
Spin period derivative, $\dot{P}$	$1.1645(1) \times 10^{-20}$			
Spin-down power, $\dot{E}$ (erg s <sup>-1</sup> )	$2.8 \times 10^{34}$			
Surface magnetic field strength, $B_S$ (G)	$1.5 \times 10^{8}$			
Light-cylinder magn. field strength, $B_{LC}$ (G)	$1.0 \times 10^{5}$			
Energy flux <sup>a</sup> , $F_{\gamma}$ (erg cm <sup>-2</sup> s <sup>-1</sup> )	$8.363 \times 10^{-12}$			
Gamma-ray luminosity, $\mathcal{L}_{\gamma}$ (erg s <sup>-1</sup> )	$4.0 \times 10^{33}$			
Gamma-ray efficiency, $\eta_{\gamma}$	14.3 per cent			

Note.  $^a$  Measured in the energy range between 100 MeV and 100 GeV, from 4FGL-DR4 (Ballet et al. 2023).

were caused by significant orbital frequency variations, we used SPIDER\_TWISTER, 8 a PYTHON-based tool designed to fold pulsar data across a range of  $T_{\rm asc}$  values, allowing for searches across multiple orbital phases. Since no significant pulsations were detected, this suggests that the non-detections are unlikely to be caused by high orbital frequency derivatives. Instead, they are more consistent with eclipses. Further supporting this interpretation is the fact that our radio timing solution is sufficiently precise for gamma-ray timing, as evidenced by the detection of gamma-ray pulsations spanning 16 yr of *Fermi* data (see Section 4).

We found a 2016 archival radio observation of this *Fermi* field with the Parkes telescope (project P814 Camilo et al. 2017). The sky position of this observation is about 1 arcmin away from the position of the pulsar and there comfortably falls within the primary beam of the telescope. We folded these data using the final gamma-ray timing solution (see Section 4) to search for radio pulsations, but none were detected. The orbital phase coverage of the observation spans from phase 0 to 0.4, corresponding to the eclipsing region based on other

observations (Fig. 3). A recent study has analysed this observation in detail (Kerr et al. 2025), but no pulsations were reported there either.

#### 4 GAMMA-RAY PULSATIONS

To search for gamma-ray pulsations from this pulsar, we used data recorded by the *Fermi* Large Area Telescope (LAT). We used SOURCE-class photons according to the 'Pass 8' P8R3\_SOURCE\_V3 instrument response functions (Atwood et al. 2013; Bruel et al. 2018) and selected photon energies similar to the 4FGL-DR4 source catalogue (Ballet et al. 2023). Each gamma-ray photon is assigned a photon weight, representing the probability the photon is from the foreground compared to the background (Bickel, Kleijn & Rice 2008; Kerr 2011; Bruel 2019). This is computed using spectral and spatial models of the gamma-ray sky using gtsrcprob. The sources' positions and spectra are taken from 4FGL-DR4 (Ballet et al. 2023), with the Galactic and diffuse emission models, g1l\_iem\_uw1216\_v13.fits and iso\_P8R3\_SOURCE\_V3\_v1.txt.

To improve computing efficiency in pulsation search and timing analysis, we performed a cut on the photon weights. The pulsation significance depends directly on these weights  $w_j$  and scales linearly with  $W^2 = \sum_j w_j^2$ . The expected value for the widely used weighted H-test statistic (Kerr 2011) is proportional to  $W^2$  (Nieder et al. 2020a), with a source-dependent prefactor describing pulse profile and background, which is typically of order unity. The scaling is used to remove the majority of low-weight photons by introducing a minimum weight  $w_{\min}$  which still retains 99 per cent of the signal. For this source, we chose  $w_{\min} = 0.01$  which reduced the number of photons by 90 per cent while preserving  $W^2 = 380$ .

The gamma-ray pulsation search was guided by the pulsar parameter values as measured in the radio timing analysis and for the likely optical counterpart. The astrometric parameters are provided to high enough precision in Gaia DR3 (Gaia Collaboration 2023) that a search over these was not required. Radio timing allowed us to fix two further parameters, the time of ascending node  $T_{\rm asc}$  and projected semimajor axis x, and to search two other parameters within their uncertainty margins, spin frequency f and orbital period  $P_{\rm orb}$ . As radio timing is usually more sensitive to eccentric orbits than gamma-ray searches and did not show signs of non-negligible eccentricity, we assumed a circular orbit in the search. We searched the spin-frequency derivative  $\dot{f}$  in the range 0 to  $-2\times 10^{-14}\,{\rm Hz~s^{-1}}$ , which is guided by the population of known MSPs.

The search was performed on a single compute node with a GPU, assuming a constant orbital period. The code searches over the f range using FFTs, while looping over a lattice of  $P_{\text{orb}}$  and f trials. The lattice is built using a parameter space metric (Nieder et al. 2020a), allowing a maximum expected signal loss of 5 per cent in the third harmonic.

The search found a H statistic maximum of H=76.3, which is statistically very significant, but much lower than expected for a pulsar with  $W^2=380$ . This could be explained by pulsar properties not accounted for by our spin-phase model. Over the course of the gamma-ray data span, pulsations in a time-versus-spin-phase plot seem to come into and out of focus several times which is typical for spider pulsars where variations of the orbital period have not been accounted for.

Quasi-random variability around a central orbital period is common among spider pulsars. These orbital period variations (OPVs) have been seen for nearly every redback pulsar (e.g. Clark et al. 2021; Burgay et al. 2024; Corcoran et al. 2024; Thongmeearkom et al.

<sup>&</sup>lt;sup>8</sup>https://github.com/alex88ridolfi/SPIDER\_TWISTER

2024), and several black-widow pulsars (e.g. Voisin et al. 2020b). This behaviour is usually thought to be a consequence of gravitational quadrupole moment variations of the pulsar's companion star (e.g. Applegate & Shaham 1994; Lazaridis et al. 2011).

The first stage of our timing code is using the sliding-window technique to provide a first model tracking the orbital period variations over time. This technique slides a window of a couple of 100 d length over the 16 yr of data and searches within these time spans over time of ascending node and orbital period offsets from the nominal central value. In this case, a 400-d window has been sufficient, being short enough that the assumption of a constant orbital period is acceptable and being long enough to accumulate sufficient S/N. The result is shown in grey-scale in Fig. 5, showing the cumulative long-term variation of the orbital period in the ascending node if compared to a constant orbital period model. This is used to fit an initial Gaussian process model.

The second stage uses the OPV model from the sliding-window method as a starting point, and then jointly refines it along with the other pulsar parameters and the gamma-ray pulse template, using both gamma-ray photons and radio TOAs. We also fit three OPV 'hyperparameters' describing the covariance function of the orbital phase variations. For the latter, we apply the commonly used Matérn covariance function (e.g. Rasmussen & Williams 2006). It is described by an amplitude, h, length scale,  $\ell$ , and a smoothness parameter, v. This covariance function models the noise power spectral density by a smoothly broken power law, being flat below a corner frequency  $f_c = \sqrt{\nu}/\sqrt{2}\pi \ell$  and breaking to a power law at higher frequencies with a spectral index of  $\Gamma = -(2\nu + 1)$ . We use a Gibbs sampling approach to deal with the multicomponent likelihood function for each photon (Thongmeearkom et al. 2024). We will present more details on these methods and a release of the code in future works which are in preparation.

The timing analysis improved the H statistic to H=627.8 with clear pulsations over the 16 yr of the *Fermi* mission and a pulse profile with two narrow peaks, roughly half a rotation apart (see Fig. 5). The resulting pulsar parameters and estimated properties are listed in Table 3.

In Fig. 6, we show the phase-aligned radio and gamma-ray pulse profiles. The phase lag between radio and gamma-ray pulses is slightly ambiguous as the separation between the two gamma-ray peaks is roughly half a rotation apart, but looks comparable to the MSP population (Smith et al. 2023; Burgay et al. 2024). A full alignment analysis could be used to estimate the binary inclination angle using emission models (e.g. Corongiu et al. 2021), but is outside the focus of this study.

## **5 X-RAY EMISSION**

An X-ray source corresponding to PSR J1544–2555 was first discovered by Mayer & Becker (2024) and classified as a likely pulsar, in a systematic cross-match between *Fermi*-LAT and SRG/eROSITA (Predehl et al. 2021) sources. The detected X-ray emission is likely to be of non-thermal origin, either in the magnetosphere, or in an intrabinary shock of the system. While the X-ray source can be considered securely detected with a detection likelihood around 20, it has a relatively low count rate of  $(3.3 \pm 0.9) \times 10^{-2}$  ct s<sup>-1</sup>, in the main eROSITA energy band 0.2–2.3 keV. This low count statistic

prohibits a detection of X-ray pulsations in the eROSITA all-sky survey, as well as the execution of detailed spectral analysis.

We briefly estimate the intrinsic X-ray luminosity of the pulsar in the following way: the observed DM of DM = 25.817 pc cm<sup>-3</sup> corresponds to an approximate X-ray absorption column density of  $N_{\rm H}=7.8\times10^{20}\,{\rm cm^{-2}}$  (He, Ng & Kaspi 2013). Assuming a power-law X-ray spectrum with a typical photon index of  $\Gamma_{\rm X}=2.0$ , this corresponds to an unabsorbed source flux of  $F=(8.0\pm2.2)\times10^{-14}\,{\rm erg\,s^{-1}\,cm^{-2}}$  in the 0.5–8.0 keV band. For the distance of 2.0 kpc, obtained from the best-fitting model of the optical light curve assuming a neutron star mass of  $1.8\,{\rm M_\odot}$  (see Section 6.2), this yields a pulsar luminosity of  $L_{\rm X}\approx4.0\times10^{31}\,{\rm erg\,s^{-1}}$ . This corresponds to an X-ray efficiency of  $L_{\rm X}/\dot{E}\approx1.4\times10^{-3}$ , which is within the typical range for X-ray emitting pulsars (e.g. Becker & Truemper 1997). Similarly, the gamma-ray to X-ray luminosity ratio  $L_{\gamma}/L_{\rm X}\approx100$  is consistent with values commonly observed in MSPs (Abdo et al. 2013).

#### 6 OPTICAL MODELLING

## 6.1 Optical modelling configuration

We used the stellar binary light-curve synthesis code, ICARUS (Breton et al. 2011) to fit the light curves of PSR J1544–2555. The code is parametrized by the mass ratio (q), orbital period  $(P_{\rm orb})$ , orbital inclination (i), rotational-to-orbital angular frequency ratio  $(\omega)$ , projected radial velocity amplitude  $(K_{\rm c})$ , filling factor  $(f_{\rm RL})$ , gravity darkening exponent  $(\beta)$ , base temperature  $(T_{\rm base})$ , irradiation temperature  $(T_{\rm irr})$ , V-band total extinction  $(A_{\rm V})$ , and distance modulus  $(\mu)$ .  $f_{\rm RL}$  is the ratio of the companion radius to the distance between the companion centre and the first Lagrangian point (L1). Modelled fluxes are evaluated from atmospheric grids which are generated from the atmospheric library, ATLAS9 (Castelli & Kurucz 2004). Full details about the procedure for creating atmospheric grids are described in Kennedy et al. (2022).

We assumed the companion to be tidally locked ( $\omega = 1$ ). The orbital period was obtained from the radio timing solution, and the projected semimajor axis (x) was used to derive other parameters in the binary mass function. Instead of fitting  $A_{\rm V}$  and  $\mu$ , we fit the colour excess, E(B-V), and distance (d). The E(B-V) value is constrained using a Gaussian-tailed flat prior, with the upper tail peaking at E(B - V) = 0.23 and a standard deviation of 0.02. These values are derived from the dust extinction map provided by Green et al. (2019), assuming the binary lies at a distance between 0.5 and 6.5 kpc. The lower limit of the prior is set at E(B - V) = 0, ensuring that the dust column density cannot drop below zero. This Gaussian-tailed flat prior approach accounts for the possibility that the observed dust column density might be lower than the upper limit due to the relatively low resolution of the dust map. Although the optical counterpart of PSR J1544-2555 is associated with a star in the latest Gaia DR3 release (Gaia Collaboration 2023), its parallax and distance have not yet been published. Therefore, we used the DM-derived distance of 1.02 kpc from the YMW16 model and the Galactic distribution of MSPs (Levin et al. 2013) to form a prior distribution for the distance. Given that black-widow companions are thought to be fully convective stars, we used a gravity darkening exponent of  $\beta = 0.08$  (Lucy & Lucy 1967). Due to the large uncertainties in radial velocity measurements, we did not include them in the fitting along with the photometry. Instead, the observed spectra were compared with modelled spectra to verify consistency, particularly in the temperatures indicated by the prominent spectral

<sup>&</sup>lt;sup>9</sup>OPVs on shorter time-scales than the window span would necessitate to search orbital frequency derivatives as well.

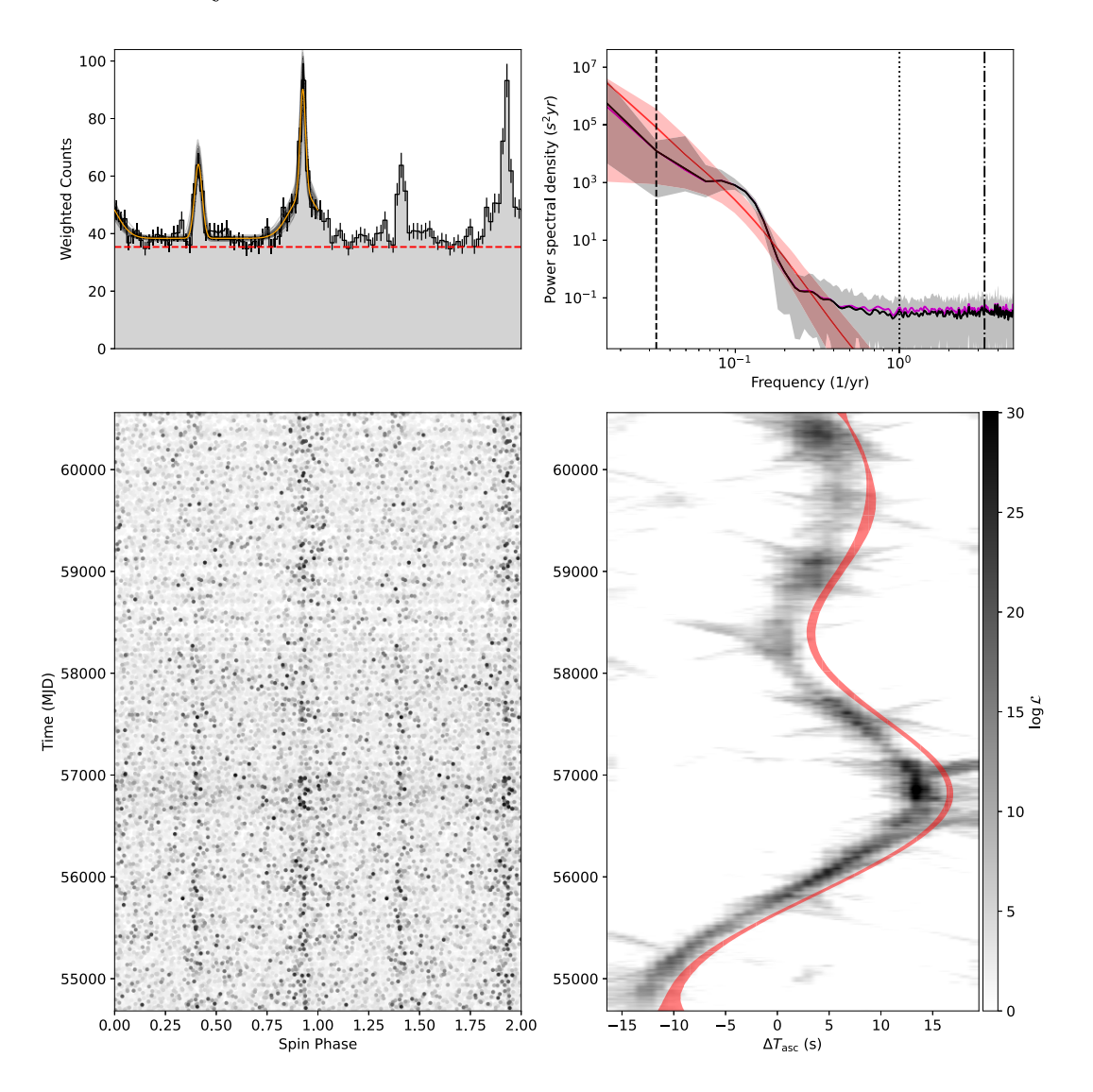


**Figure 5.** Gamma-ray pulsations and variations of the orbital phase over time for PSR J1544–2555. The panels on the left show the weighted pulsar spin phases for each gamma-ray photon for the highest-likelihood timing solution (lower panel) and the integrated pulse profile (upper panel). The solid orange curve represents the associated highest-likelihood pulse-profile template and the 100 faint black curves are randomly drawn samples from the Monte Carlo analysis to visualize the uncertainty on the pulse-profile template. The bottom-right panel shows the orbital phase variations as a function of time. The grey-scale image shows the log-likelihood for offsets from the pulsar's  $T_{\rm asc}$  as measured in overlapping 400-d windows. The red shaded curves represent the 95 per cent confidence interval on those deviations, obtained from Monte Carlo timing analysis, with a 3 s-offset for clarity. The top-right panel shows the power spectral density of the orbital phase variations. The red shaded region illustrates the 95 per cent confidence interval of the Matérn model. The black solid curve shows the estimated power spectrum from the joint radio and gamma-ray fitting and the grey shaded region its 95 per cent confidence interval. The purple solid curve, mostly hidden behind the black one, shows the power spectrum estimated from gamma-ray timing alone.

lines. To improve parameter constraints, we fit the data with a fixed pulsar mass ranging from 0.6 to  $3.6\,M_\odot$ , in increments of  $0.2\,M_\odot$ .

We initially fitted the observed light curves with the direct heating (DH) model where the irradiation incident on the companion is immediately reprocessed and re-emitted (Breton et al. 2013). However, these light curves exhibit slight asymmetries when compared to the modelled curves, as shown in Fig. 7. To address these discrepancies, we also fitted the data using convection (C), diffusion-and-convection (D + C), and spot models. The C and D + C models are heat redistribution models that include both diffusion and convection terms, as described in Voisin et al. (2020c). The diffusion term is parametrized by the diffusion coefficient  $\kappa$ , while the convection term is parametrized by a coefficient  $\nu_c$  within a uniform angular velocity profile. The spot model is based on a model of high-energy particles

directed toward the magnetic pole of its companion (Sanchez & Romani 2017). Our spot model builds upon the direct heating model by introducing a Gaussian temperature profile centred at ( $\phi_{\rm spot}$ ,  $\theta_{\rm spot}$ ), with a radius  $r_{\rm spot}$  and a temperature scaling factor  $T_{\rm spot}$ . Model optimization was performed using PYMULTINEST (Buchner et al. 2014), a PYTHON wrapper for the multinest library (Feroz, Hobson & Bridges 2009), which implements the nested sampling algorithm for Bayesian inference.

We calibrated the absolute flux of the observed light curves using *g*- and *r*-band data from the Panoramic Survey Telescope and Rapid Response System (Pan-STARRS) Data Release 2 (Magnier et al. 2020) and *u*-band data from the SkyMapper Southern Survey (SMSS) Data Release 4 (Onken et al. 2024). Discrepancies in magnitude calibration between different instruments and filter systems could

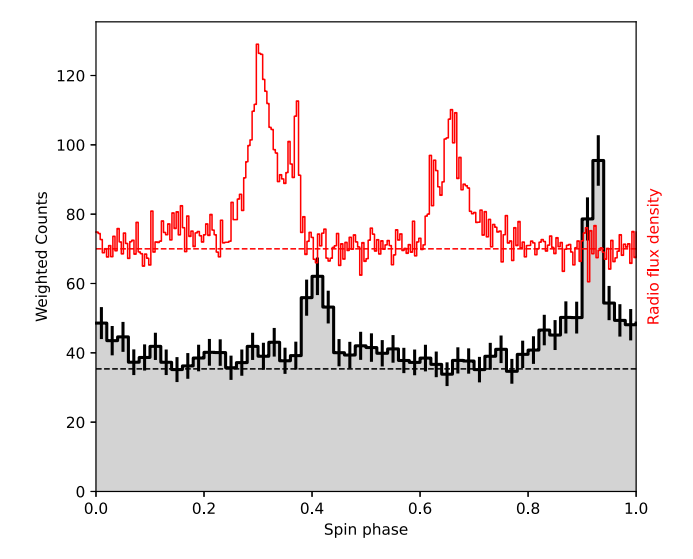


**Figure 6.** Phase-aligned radio (top) and gamma-ray (bottom) pulse profiles for PSR J1544–2555. The radio profile based on MeerKAT UHF observations is shown in arbitrary flux density units from an arbitrary background level (dashed line).

introduce small systematic deviations from the true flux of the star. To address this, we allowed the generated light curves to adjust within a Gaussian prior with a standard deviation of 0.05 mag.

#### 6.2 Optical modelling results and discussions

The parameter constraints in heat redistribution models are similar to those in the direct heating model, despite slightly better Bayesian evidence for the former. In contrast, the spot model exhibits a significantly improved goodness of fit and distinct parameter constraints compared to the other three models. Specifically, the spot model suggests an inclination angle of approximately 65°, consistent across different pulsar masses (Fig. 8), while the other models constrain the inclination to around 46°-50°. Due to the lack of precise radial velocity data,  $K_c$ , the component masses could not be determined with high accuracy. Given that pulsar masses typically range between 1.0 and 2.1  $M_{\odot}$ ,  $K_c$  is likely between 400 and 500 km s<sup>-1</sup> for the spot model and  $300-400 \, \mathrm{km \, s^{-1}}$  for the other models. The companion mass is estimated to be between 0.06 and 0.1  $M_{\odot}$  for the spot model, and  $0.08-0.12~M_{\odot}$  for the other models. Multiband optical data, a large temperature contrast between the day and night sides of the companion, and precise radio ephemeris provide strong constraints on temperature parameters, resolving their degeneracy with distance and Roche lobe filling. The fitted parameters for  $T_{\text{base}}$  and  $T_{\text{irr}}$  are approximately 1800 K and 6600-6700 K, respectively. Averaging the flux from the day and night hemispheres yields  $T_{\rm day} \sim 6000$ -6200 K and  $T_{\rm night} \sim 2300$  K. The constrained distance range is 1.7-2.0 kpc, which exceeds the predicted DM distances from the YMW16 and NE2001 models. Table 4 reports the fitted and derived parameters from the spot model assuming a neutron star mass of 1.8  $M_{\odot}$ , corresponding to a value close to the median neutron star mass seen in redback systems (Strader et al. 2019). The corresponding posterior distributions of the spot model parameters are shown in Figure A2.

The spectra, taken between orbital phases 0.5 and 1.0 (near the light curve maximum), are dominated by noise. After smoothing them using a boxcar filter, we identified prominent lines such as Ca II K and H, CH, and weaker H Balmer lines, as shown in Fig. A1. These

lines are typical features of G-type stars whose effective temperatures are 5000–6000 K. The companion's effective average temperature from the spot model, as shown in Fig. 9, during the orbital phases between 0.5 and 1.0, also falls in the same temperature range.

The light curve near the maximum is less asymmetric compared to the orbital phases around the minimum, unlike other known blackwidows, where asymmetry is typically more pronounced near the peak. The light curve also shows a bluer colour near the minimum, as depicted in Fig. 7. Of the four models fitted to the data, only the spot model accurately captures the observed light curves, particularly near the minimum. This model suggests a spot near the pole with a maximum temperature exceeding 8000 K and a width (corresponding to the standard deviation of the Gaussian spot profile) of about 8°.

A similar phenomenon, in which light curves appear bluer around the minima, was also observed in PSR J1653–0158 (Romani, Filippenko & Cenko 2014). This effect is attributed to non-thermal emission, such as synchrotron radiation from intrabinary shocks. This emission makes the spectra appear bluer around the minima, when the companion's blackbody radiation is at its faintest. The asymmetry in the light curve is likely due to the geometry of the shocks. This could also explain the similar effect observed in the companion of PSR J1544–2555.

Although the spot model provides the best fit, no emission lines were detected that could originate from either a hotspot or an intrabinary shock. To distinguish between these two scenarios, one could fit a model combining direct heating with a non-thermal component, as implemented in Nieder et al. (2020b), or obtain X-ray spectra to check for synchrotron emission.

#### 6.3 Comparison with previous work

When comparing our results with the modelling presented by Karpova et al. (2024, hereafter K24), several caveats must be considered. K24 adopted a direct heating model that does not account for gravity darkening. In addition, the quality and coverage of their light curve data differs from ours. Notably, their data set lacks coverage around the orbital minimum, which significantly weakens constraints on  $T_{\text{base}}$ . The colour coverage is also non-uniform, with a paucity of data in the V and B bands. This limits the reconstruction of a consistent temperature profile across orbital phase and introduces degeneracies that propagate into key system parameters, such as the orbital inclination and Roche lobe filling factor.

Despite these limitations, we perform a comparison between the K24 parameters and those derived from our best-fitting model, transforming quantities as needed to match the ICARUS framework. Following Zharikov et al. (2019), we adopt the assumption  $T_{\text{night}} = T_{\text{base}}$  and use the relation

$$T_{\rm day} = T_{\rm night} \times \left(1 + \frac{F_{\rm in}}{\Delta S \sigma T_{\rm night}^4}\right)^{1/4},\tag{1}$$

where  $\sigma$  denotes the Stefan–Boltzmann constant, and  $F_{\rm in}$  denotes the effective flux received from the pulsar by a surface element  $\Delta S$  on the companion's irradiated hemisphere. Using the maximum 'day-side' temperature  $T_{\rm day,max}$  reported by K24, we compute the equivalent  $T_{\rm irr}$  in the ICARUS context by subtracting the fourth power of  $T_{\rm night}$  from that of  $T_{\rm day,max}$ . This value corresponds to  $T_{\rm irr}$  at the 'nose' of the star, where the irradiation is maximal.

To compare with the parameter definition in ICARUS, which evaluates  $T_{\rm irr}$  with respect to the companion's centre of mass, we account for the geometry of the system, specifically the separation between the pulsar and companion, and the companion's

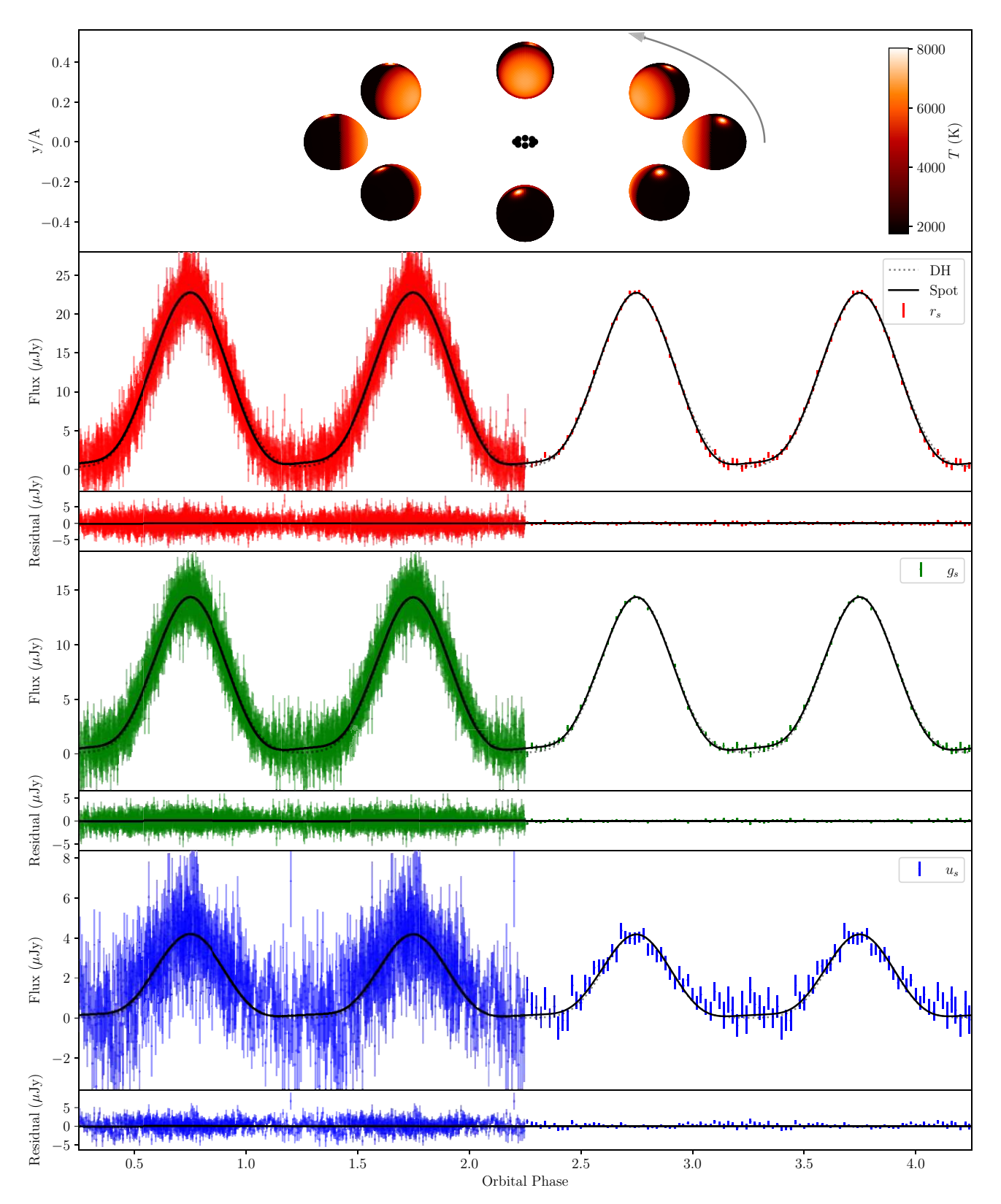
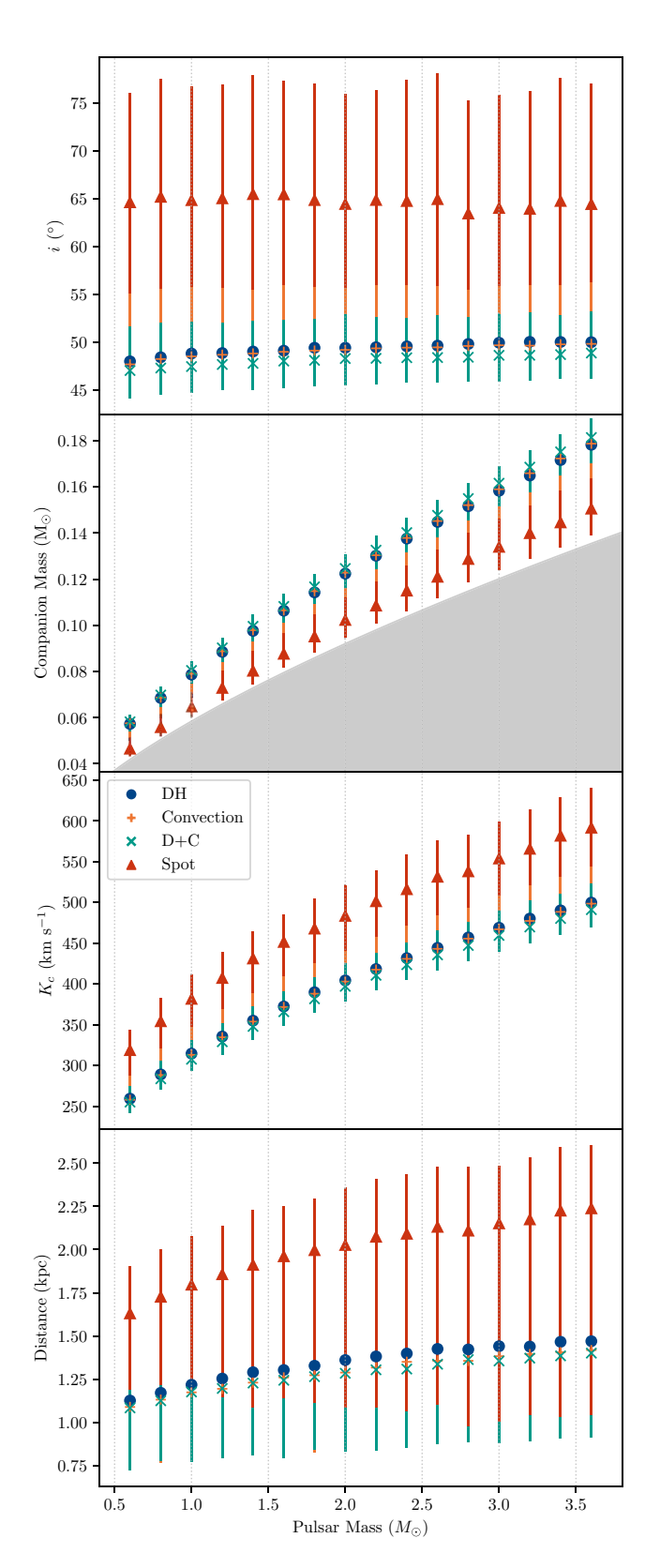


Figure 7. The schematic model of PSR J1544-2555's companion with the spot model is shown in the uppermost panel. The subsequent panels display the light curves in  $r_s$ ,  $g_s$ , and  $u_s$ , respectively. The observed data are presented for the first two cycles. These light curves are binned using an orbital phase interval of 0.02 and are shown in cycles 3 and 4.



**Figure 8.** Parameter constraints of the four models against pulsar masses. The vertical bars represent the 95 per cent confidence intervals of posterior distributions. The shaded area denotes the forbidden parameter region ( $i > 90^{\circ}$ ).

**Table 4.** Fitted and derived parameters from the spot model after fixing  $M_{\rm psr}$  to 1.8  ${\rm M}_{\odot}$ .  $T_{\rm day}$  and  $T_{\rm night}$  are the average temperatures of the companion's hemispheres facing towards and away from the pulsar, respectively.  $T_{\rm dush}$  and  $T_{\rm dawn}$  are the average temperatures of the eastern and western hemispheres of the companion, respectively.

Parameter	Value		
Fitted parameters			
Colour excess, $E(B-V)$	$0.21^{+0.04}_{-0.08}$		
Companion radial velocity semi-amplitude, $K_c$ (km s <sup>-1</sup> )	$470^{+20}_{-20}$		
Distance, d (kpc)	$2.0^{+0.1}_{-0.3}$		
Orbital inclination, $i$ ( $^{\circ}$ )	$65^{+6}_{-5}$		
Base temperature, $T_{\text{base}}$ (K)	$1700^{+600}_{-500}$		
Irradiation temperature, $T_{irr}$ (K)	$6700^{+300}_{-300}$		
Roche lobe filling factor, $f_{RL}$	$0.65^{+0.05}_{-0.1}$		
Spot longitude, $\phi_{ m spot}$ ( $^{\circ}$ )	$-130^{+10}_{-8}$		
Spot colatitude, $\theta_{\rm spot}$ ( $^{\circ}$ )	$30^{+10}_{-10}$		
Angular radius of the spot, $R_{\rm spot}$ (°)	$8^{+3}_{-2}$		
Spot temperature, $T_{\text{spot}}$ (K)	$6600^{+1000}_{-900}$		
Derived parameters			
Mass ratio, q	$18.9^{+0.9}_{-0.9}$		
Companion mass, $M_c$ ( $M_{\odot}$ )	$0.095^{+0.005}_{-0.004}$		
Dusk-side temperature, $T_{\text{dusk}}$ (K)	$4500^{+200}_{-200}$		
Day-side temperature, $T_{\rm day}$ (K)	$6100^{+200}_{-300}$		
Dawn-side temperature, $T_{\text{dawn}}$ (K)	$4400^{+200}_{-200}$		
Night-side temperature, $T_{\text{night}}$ (K)	$2300^{+300}_{-300}$		
Companion radius, $R_c$ ( $R_{\odot}$ )	$0.171^{+0.008}_{-0.02}$		
Volume-averaged filling factor, $f_{\rm VA}$	$0.83^{+0.05}_{-0.1}$		

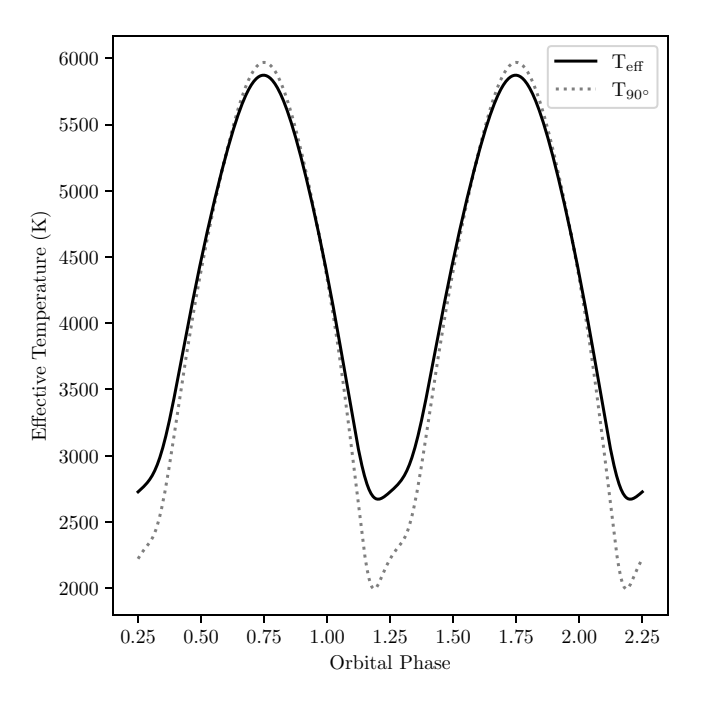


**Figure 9.** The flux-averaged temperature of the companion's hemisphere facing Earth is represented by the black solid line, indicating the effective temperature as inferred for the system's actual inclination. For comparison, the dotted grey line shows the flux-averaged temperature assuming the binary is viewed edge-on. This comparison highlights how the inclination angle affects the observed temperature distribution due to changes in the projected area and visibility of heated regions on the companion's surface.

radius measured from its centre of mass toward the pulsar. Applying this correction yields an equivalent  $T_{\rm irr} \approx 6570$  K, consistent with our best-fitting model. Other parameters such as the mass ratio, distance, and Roche lobe filling factor also show good agreement.

However, the inclination and  $T_{\rm night}$  values reported by K24 are both higher than those found in our best-fitting model. This is likely attributable to the absence of data near the orbital minimum in their light curve, which reduces sensitivity to the flux contribution from the night side. As a result, their modelling likely overestimates  $T_{\rm night}$ , and to reproduce the observed modulation amplitude, a correspondingly higher inclination is required. This degeneracy between  $T_{\rm night}$  and inclination can be broken with multiband observations such as those presented in this work.

## 7 CONCLUSIONS

In this work, we have presented the discovery of a new black-widow millisecond pulsar, PSR J1544–2555, associated with the *Fermi*-LAT source 4FGL J1544.2–2554. This discovery adds to the growing catalogue of known black-widow pulsars and highlights the value of multiwavelength observations in the search for spider pulsar systems.

Optical observations conducted with ULTRACAM revealed a  $\sim$ 2.7 h orbital periodicity, consistent with black-widow systems. This ephemeris enabled a targeted 1-h MeerKAT radio observation, optimized to avoid orbital phases prone to radio eclipses. We identified radio pulsations in an acceleration search on 15-min segments, confirming the presence of a millisecond pulsar with a spin period of  $\sim$ 2.4 ms. We derived a preliminary timing solution from a radio timing campaign with the Murriyang Parkes telescope, the Effelsberg 100-m radio telescope, and the Nançay Radio Telescope, which enabled us to detect gamma-ray pulsations in the Fermi-LAT data. A full 16-yr timing solution was obtained, allowing us to track orbital period variations. Furthermore, the associated X-ray source detected with eROSITA in the energy bands 0.2-2.3 and 2.3-5.0 keV, first discovered by Mayer & Becker (2024), though limited by the low count rates, provides additional confirmation of the source's non-thermal emission, characteristic of black-widow systems.

Optical light curve modelling with ICARUS favours a spot model, which effectively captured asymmetries around the minimum. This feature, along with the observed bluer colours at minimum, suggests potential non-thermal emission from intrabinary shocks. Further observations, including detailed X-ray spectroscopy, will be required to confirm this hypothesis. The quality of the spectra was insufficient for radial velocity measurements, preventing the determination of the neutron star's mass. Future high-resolution spectroscopic studies could provide the radial velocity data needed to disentagle between heating models, thus allowing to refine system parameters and ultimately measure the neutron star's mass.

The discovery of PSR J1544-2555 exemplifies the utility of the *Fermi*-LAT catalogue in identifying MSP candidates and underscores the importance of optical surveys in detecting variable sources that can be effectively followed up through targeted radio observations.

# **ACKNOWLEDGEMENTS**

The authors would like to thank Soheb Mandhai and Pengyue Sun for their help with conducting optical observations.

The MeerKAT telescope is operated by the South African Radio Astronomy Observatory (SARAO), which is a facility of the National

Research Foundation, an agency of the Department of Science and Innovation. We thank staff at SARAO for their help with observations and commissioning. TRAPUM observations used the FBFUSE and APSUSE computing clusters for data acquisition, storage, and analysis. These clusters were funded and installed by the Max-Planck-Institut für Radioastronomie (MPIfR) and the Max-Planck-Gesellschaft. The National Radio Astronomy Observatory is a facility of the National Science Foundation operated under cooperative agreement by Associated Universities, Inc. The Parkes radio telescope is part of the Australia Telescope National Facility (https://ror.org/05qajvd42) which is funded by the Australian Government for operation as a National Facility managed by CSIRO. We acknowledge the Wiradjuri people as the traditional owners of the Observatory site. The Nançay Radio Observatory is operated by the Paris Observatory, associated with the French Centre National de la Recherche Scientifique (CNRS) and Université d'Orléans. It is partially supported by the Region Centre Val de Loire in France.

The Fermi LAT Collaboration acknowledges generous ongoing support from a number of agencies and institutes that have supported both the development and the operation of the LAT as well as scientific data analysis. These include the National Aeronautics and Space Administration and the Department of Energy in the United States, the Commissariat à l'Energie Atomique and the Centre National de la Recherche Scientifique / Institut National de Physique Nucléaire et de Physique des Particules in France, the Agenzia Spaziale Italiana and the Istituto Nazionale di Fisica Nucleare in Italy, the Ministry of Education, Culture, Sports, Science and Technology (MEXT), High Energy Accelerator Research Organization (KEK), and Japan Aerospace Exploration Agency (JAXA) in Japan, and the K. A. Wallenberg Foundation, the Swedish Research Council and the Swedish National Space Board in Sweden.

This work has made use of data from the European Space Agency (ESA) mission *Gaia* (https://www.cosmos.esa.int/gaia), processed by the *Gaia* Data Processing and Analysis Consortium (DPAC, https://www.cosmos.esa.int/web/gaia/dpac/consortium). Funding for the DPAC has been provided by national institutions, in particular the institutions participating in the *Gaia* Multilateral Agreement.

TT is grateful to the National Astronomical Research Institute of Thailand (NARIT) for awarding a student scholarship. RPB acknowledges support from the European Research Council (ERC) under the European Union's Horizon 2020 research and innovation programe (grant agreement No. 715051; Spiders). SBD acknowledges the support of a Science and Technology Facilities Council (STFC) stipend (grant number: ST/X001229/1) to permit work as a postgraduate researcher. ECF was supported by NASA under award number 80GSFC24M0006. ULTRACAM and VSD are supported by STFC. Lastly, we would like to thank Lucas Guillemot for reviewing the manuscript on behalf of the *Fermi*-LAT Collaboration.

# DATA AVAILABILITY

TRAPUM and ULTRACAM observations are available upon reasonable request to the corresponding author. Reduced and calibrated optical light curves are available in accompanying online material. The *Fermi*-LAT data are available from the *Fermi* Science Support Center (FSSC; http://fermi.gsfc.nasa.gov/ssc). Gamma-ray timing solutions are also available from the FSSC (https://fermi.gsfc.nasa.gov/ssc/data/access/lat/ephems/).

## REFERENCES

```
Abdo A. A. et al., 2010, ApJS, 188, 405
```

Abdo A. A. et al., 2013, ApJS, 208, 17

Abdollahi S. et al., 2020, ApJS, 247, 33

Alpar M. A., Cheng A. F., Ruderman M. A., Shaham J., 1982, Nature, 300, 728

Applegate J. H., Shaham J., 1994, ApJ, 436, 312

Archibald A. M. et al., 2009, Science, 324, 1411

Arons J., Tavani M., 1993, ApJ, 403, 249

Arzoumanian Z., Fruchter A. S., Taylor J. H., 1994, ApJ, 426, L85

Atwood W. B. et al., 2009, ApJ, 697, 1071

Atwood W. et al., 2013, in Brandt T. J., Omodei N., Wilson-Hodge C., eds, Proc. 4th Fermi Symposium, Monterey, California, 2012 (eConf C121028), NASA, Washington, DC, USA, p. 8

Backer D. C., Kulkarni S. R., Heiles C., Davis M. M., Goss W. M., 1982, Nature, 300, 615

Backer D. C., Kulkarni S. R., Taylor J. H., 1983, Nature, 301, 314

Ballet J., Bruel P., Burnett T. H., Lott B., The Fermi-LAT collaboration, 2023, preprint, (arXiv:2307.12546)

Barr E., 2020, Astrophysics Source Code Library, record ascl:2001.014

Becker W., Truemper J., 1997, A&A, 326, 682

Bhattacharya D., van den Heuvel E., 1991, Phys. Rep., 203, 1

Bickel P., Kleijn B., Rice J., 2008, ApJ, 685, 384

Breton R. P., Rappaport S. A., van Kerkwijk M. H., Carter J. A., 2011, ApJ, 748, 115

Breton R. P. et al., 2013, ApJ, 769, 108

Bruel P., 2019, A&A, 622, A108

Bruel P., Burnett T. H., Digel S. W., Johannesson G., Omodei N., Wood M., 2018, preprint (arXiv:1810.11394)

Buchner J. et al., 2014, A&A, 564, A125

Burgay M. et al., 2024, A&A, 691, A315

Camilo F., Ransom S., Ray P., Kerr M., Ferrara E., 2017, Parkes observations for project P814 semester 2016OCTS

Castelli F., Kurucz R. L., 2004, A&A, 419, 725

Clark C. J. et al., 2021, MNRAS, 502, 915

Clark C. J. et al., 2023a, Nat. Astron., 7, 451

Clark C. J. et al., 2023b, MNRAS, 519, 5590

Corcoran K. A. et al., 2024, preprint (arXiv:2412.08688)

Cordes J. M., Lazio T. J. W., 2002, preprint (astro-ph/0207156)

Corongiu A. et al., 2021, MNRAS, 502, 935

Damour T., Taylor J. H., 1991, ApJ, 366, 501

Dhillon V. S. et al., 2007, MNRAS, 378, 825

Dhillon V. S. et al., 2021, MNRAS, 507, 350

Djorgovski S., Evans C. R., 1988, ApJ, 335, L61

Feroz F., Hobson M. P., Bridges M., 2009, MNRAS, 398, 1601

Frail D. A., Jagannathan P., Mooley K. P., Intema H. T., 2016, ApJ, 829, 119

Frail D. A. et al., 2018, MNRAS, 475, 942

Fruchter A. S., Stinebring D. R., Taylor J. H., 1988, Nature, 333, 237

Gaia Collaboration, 2023, A&A, 674, A1

Green G. M., Schlafly E., Zucker C., Speagle J. S., Finkbeiner D., 2019, ApJ, 887, 93

Guillemot L., Cognard I., van Straten W., Theureau G., Gérard E., 2023, A&A, 678, A79

He C., Ng C. Y., Kaspi V. M., 2013, ApJ, 768, 64

Hobbs G. B., Edwards R. T., Manchester R. N., 2006, MNRAS, 369, 655

Jankowski F., van Straten W., Keane E. F., Bailes M., Barr E. D., Johnston S., Kerr M., 2017, MNRAS, 473, 4436

Johnston H. M., Kulkarni S. R., 1991, ApJ, 368, 504

Jonas J., MeerKAT Team, 2016, MeerKAT Science: On the Pathway to the SKA, SARAO, Cape Town, South Africa, p. 1

Karpova A. V., Zharikov S. V., Zyuzin D. A., Kirichenko A. Y., Shibanov Y. A., Márquez I. F., 2024, A&A, 693, A158 (K24)

Keith M. J. et al., 2010, MNRAS, 409, 619

Kennedy M. R. et al., 2022, MNRAS, 512, 3001

Kerr M., 2011, ApJ, 732, 38

Kerr M. et al., 2025, ApJ, 984, 180

Kong A. K. H. et al., 2012, ApJ, 747, L3

Lazaridis K. et al., 2011, MNRAS, 414, 3134

Levin L. et al., 2013, MNRAS, 434, 1387

Li K.-L., Kong A. K. H., Hou X., Mao J., Strader J., Chomiuk L., Tremou E., 2016, ApJ, 833, 143

Linares M., Miles-Páez P., Rodríguez-Gil P., Shahbaz T., Casares J., Fariña C., Karjalainen R., 2017, MNRAS, 465, 4602

Linares M., Shahbaz T., Casares J., 2018, ApJ, 859, 54

Lomb N. R., 1976, Ap&SS, 39, 447

Lu C., Ren L., Lin J., Huang W., Yang H., Tam P. H. T., 2024, ApJ, 978, 106

Lucy L. B., Lucy B. L., 1967, Zeitschrift für Astrophysik, 65, 89

Lyne A. G. et al., 1990, Nature, 347, 650

Magnier E. A. et al., 2020, ApJS, 251, 6

Manchester R. N. et al., 2001, MNRAS, 328, 17

Mata Sánchez D. et al., 2023, MNRAS, 520, 2217

Mayer M. G. F., Becker W., 2024, A&A, 684, A208

Morello V. et al., 2018, MNRAS, 483, 3673

Nieder L., Allen B., Clark C. J., Pletsch H. J., 2020a, ApJ, 901, 156

Nieder L. et al., 2020b, ApJ, 902, L46

Oke J. B. et al., 1995, PASP, 107, 375

Onken C. A., Wolf C., Bessell M. S., Chang S.-W., Luvaul L. C., Tonry J. L., White M. C., Da Costa G. S., 2024, PASA, 41, e061

Özel F., Freire P., 2016, ARA&A, 54, 401

Papitto A. et al., 2013, Nature, 501, 517

Parkinson P. M. S., Xu H., Yu P. L. H., Salvetti D., Marelli M., Falcone A. D., 2016, ApJ, 820, 8

Perez K. I., Bogdanov S., Halpern J. P., Gajjar V., 2023, ApJ, 952, 150

Perley D. A., 2019, PASP, 131, 084503

Pletsch H. J. et al., 2012, Science, 338, 1314

Polzin E. J., Breton R. P., Bhattacharyya B., Scholte D., Sobey C., Stappers B. W., 2020, MNRAS, 494, 2948

Predehl P. et al., 2021, A&A, 647, A1

Ransom S., 2011, Astrophysics Source Code Library, record ascl:1107.017

Rasmussen C. E., Williams C. K. I., 2006, Gaussian Processes for Machine Learning, MIT Press, Cambridge, MA, USA

Ray P. S. et al., 2012, preprint (arXiv:1205.3089)

Ray P. S. et al., 2020, Res. Notes Am. Astron. Soc., 4, 37

Roberts M. S. E., 2012, Proc. Int. Astron. Un., 8, 127

Roberts M. S. E., Burgay M., D'Amico N., Esposito P., Pellizzoni A., Possenti A., 2011, Radio Pulsars: An Astrophysical Key to Unlock the Secrets of the Universe, Vol 1375, AIP, Melville, New York, USA, p. 127

Romani R. W., Shaw M. S., 2011, ApJ, 743, L26

Romani R. W., Filippenko A. V., Cenko S. B., 2014, ApJ, 793, L20

Romani R. W., Filippenko A. V., Cenko S. B., 2015, ApJ, 804, 115

Romani R. W., Kandel D., Filippenko A. V., Brink T. G., Zheng W., 2021, ApJ, 908, L46

Romani R. W., Kandel D., Filippenko A. V., Brink T. G., Zheng W., 2022, ApJ, 934, L17

Sanchez N., Romani R. W., 2017, ApJ, 845, 42

Scargle J. D., 1982, ApJ, 263, 835

Shklovskii I. S., 1970, Soviet Ast., 13, 562

Smith D. A. et al., 2023, ApJ, 958, 191

Stappers B. W. et al., 2014, ApJ, 790, 39

Strader J. et al., 2019, ApJ, 872, 42

Tarenghi M., 1986, in Barr L. D., ed., Proc. SPIE Conf. Ser. Vol. 628, Advanced Technology Optical Telescopes III. SPIE, Bellingham, p. 213

Thongmeearkom T. et al., 2024, MNRAS, 530, 4676

van Kerkwijk M. H., Breton R. P., Kulkarni S. R., 2011, ApJ, 728, 95

Voisin G., Breton R. P., Summers C., 2020a, MNRAS, 492, 1550

Voisin G., Clark C. J., Breton R. P., Dhillon V. S., Kennedy M. R., Mata-Sánchez D., 2020b, MNRAS, 494, 4448

Voisin G., Kennedy M. R., Breton R. P., Clark C. J., Mata-Sánchez D., 2020c, MNRAS, 499, 1758

Wijnands R., van der Klis M., 1998, Nature, 394, 344

Yao J. M., Manchester R. N., Wang N., 2017, ApJ, 835, 29

Zharikov S., Kirichenko A., Zyuzin D., Shibanov Y., Deneva J. S., 2019, MNRAS, 489, 5547

# SUPPORTING INFORMATION

Supplementary data are available at MNRAS online.

Please note: Oxford University Press is not responsible for the content or functionality of any supporting materials supplied by the authors. Any queries (other than missing material) should be directed to the corresponding author for the article.

APPENDIX A: THE MODELLED SPECTRA AND THE POSTERIOR DISTRIBUTIONS OF THE OPTICAL MODELLING

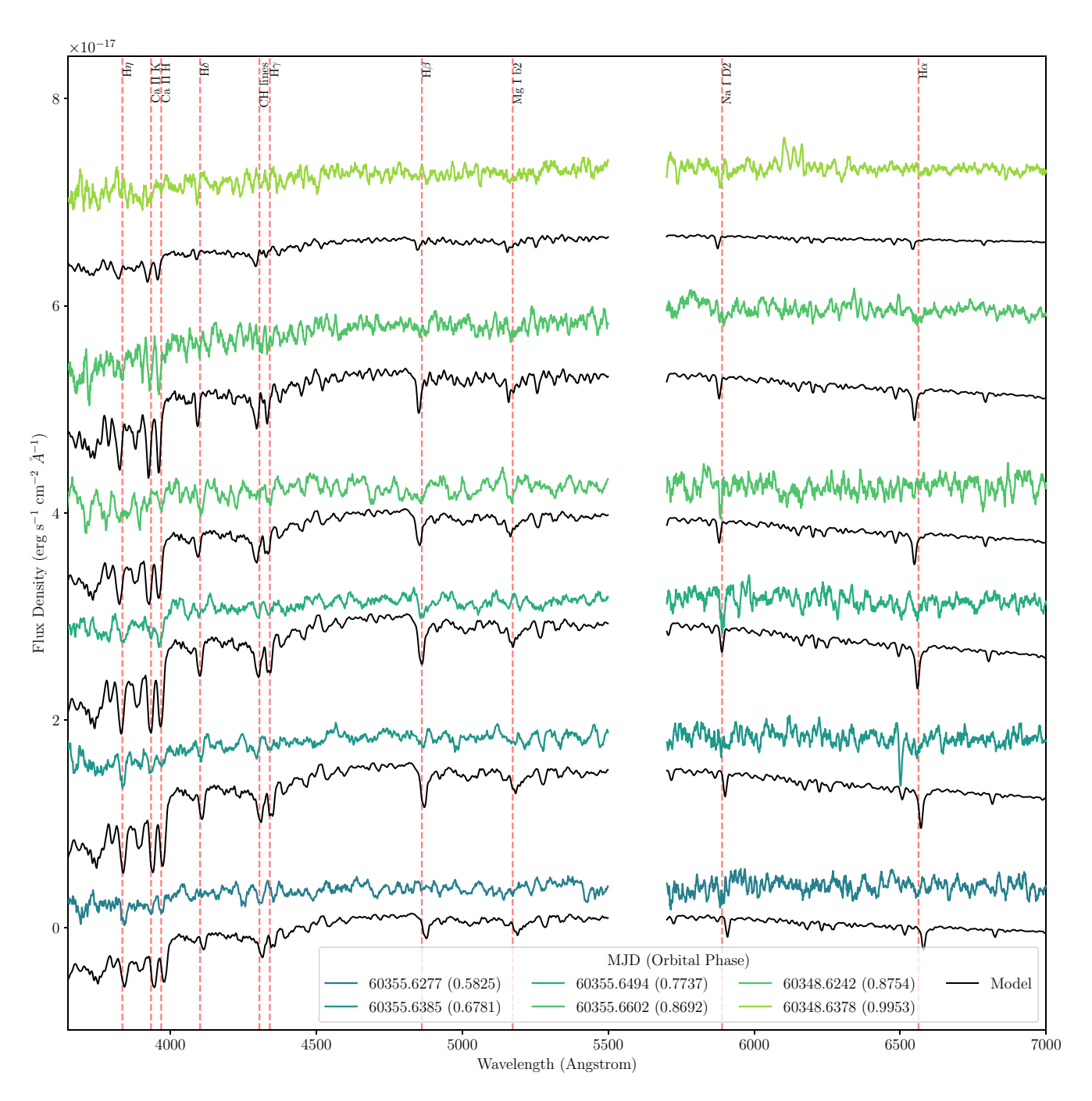


Figure A1. Observed spectra are plotted with an offset between them. The simulated spectra from the spot model using ICARUS are shown below its counterpart observed spectra. Both types of spectra are convolved with a boxcar filter (width = 9) to smooth out the noise and see lines better. Notable absorption lines are labelled at the top of the plot.

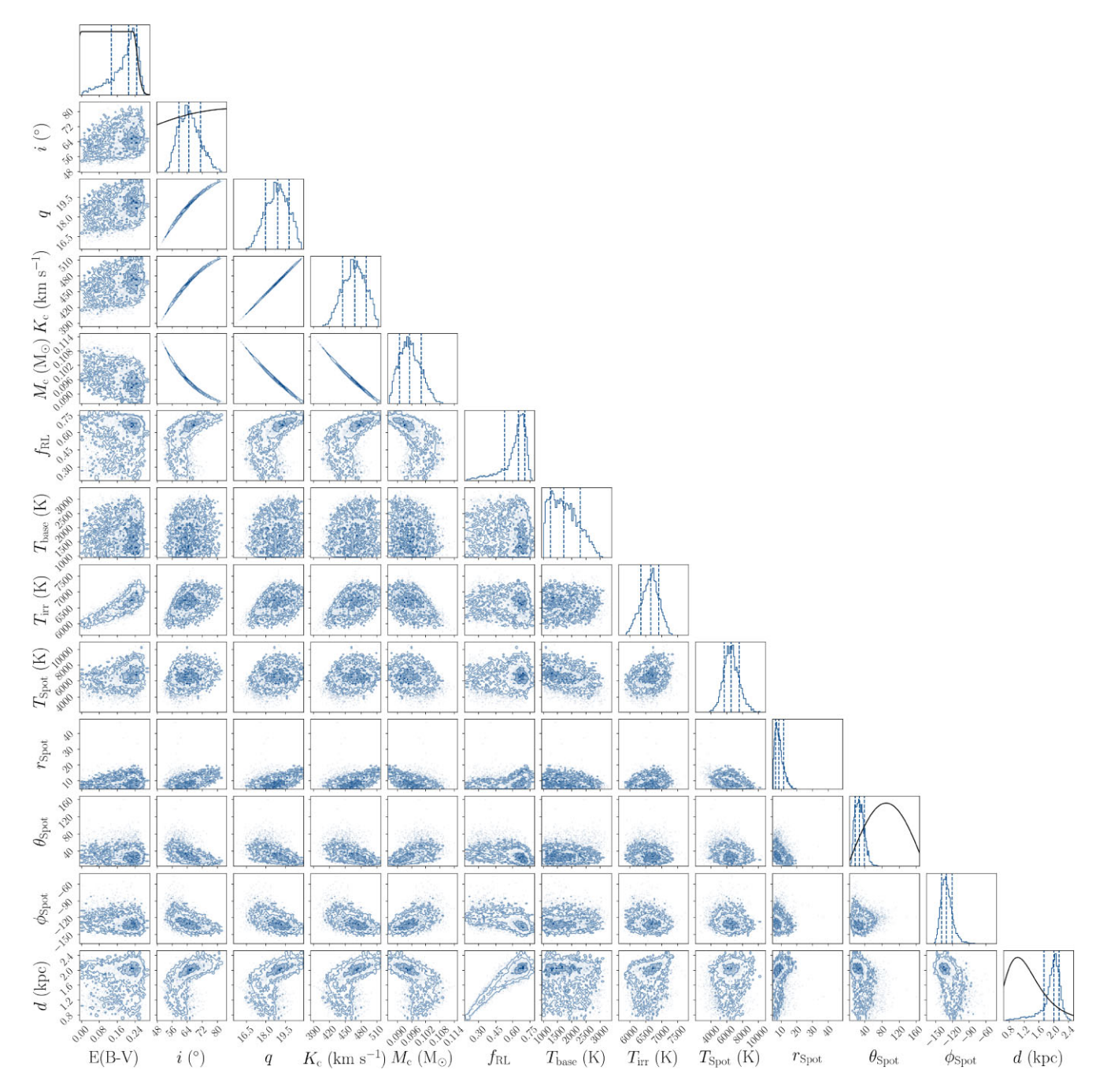


Figure A2. Corner plots displaying the various posterior distributions of the spot model where pulsar mass is fixed to 1.8  $M_{\odot}$ . The black curves in the 1D distributions show the priors distributions that were adopted.

- <sup>1</sup>Jodrell Bank Centre for Astrophysics, Department of Physics and Astronomy, The University of Manchester, Manchester M13 9PL, UK
- <sup>2</sup>National Astronomical Research Institute of Thailand, Don Kaeo, Mae Rim, Chiang Mai 50180, Thailand
- <sup>3</sup>INAF Osservatorio Astronomico di Cagliari, via della Scienza 5, I-09047 Selargius (CA), Italy
- <sup>4</sup>Max Planck Institute for Gravitational Physics (Albert Einstein Institute), D-30167 Hannover, Germany
- <sup>5</sup>Leibniz Universität Hannover, D-30167 Hannover, Germany
- <sup>6</sup>Max-Planck Institut für Extraterrestrische Physik, Giessenbachstrasse, D-85741 Garching, Germany
- <sup>7</sup>Dr. Karl Remeis-Sternwarte and Erlangen Centre for Astroparticle Physics, Friedrich-Alexander Universität Erlangen-Nürnberg, Sternwartstrasse 7, D-96049 Bamberg, Germany
- <sup>8</sup>Max-Planck-Institut für Radioastronomie, Auf dem Hügel 69, D-53121 Bonn, Germany
- <sup>9</sup>South African Radio Astronomy Observatory, 2 Fir Street, Cape Town 7925, South Africa

- <sup>10</sup>Department of Astronomy, California Institute of Technology, 1200 East California Blvd, Pasadena, CA 91125, USA
- <sup>11</sup>Astrophysics Research Cluster, School of Mathematical and Physical Sciences, University of Sheffield, Sheffield S3 7RH, UK
- <sup>12</sup>Instituto de Astrofísica de Canarias, E-38205 La Laguna, Tenerife, Spain
   <sup>13</sup>Department of Astronomy, University of Maryland, College Park, MD
   20742, USA
- <sup>14</sup>Center for Research and Exploration in Space Science & Technology II (CRESST II), NASA/GSFC, Greenbelt, MD 20771, USA
- <sup>15</sup>NASA Goddard Space Flight Center, Greenbelt, MD 20771, USA
- 16LPC2E Université d'Orléans / CNRS, F-45071 Orléans Cedex 2, France
   17 Observatoire Radioastronomique de Nançay (ORN), Observatoire de Paris, Université PSL, Univ Orléans, CNRS, F-18330 Nançay, France
- <sup>18</sup>School of Physics, Kane Building, University College Cork, Cork T12 K8AF, Ireland
- <sup>19</sup>Centre for Extragalactic Astronomy, Department of Physics, Durham University, South Road, Durham DH1 3LE, UK

This paper has been typeset from a  $T_{\hbox{\sc E}}X/\hbox{\sc LMT}_{\hbox{\sc E}}X$  file prepared by the author.